Dynamic Terrestrial Self-Righting with a Minimal Tail

Carlos S. Casarez[1] and Ronald S. Fearing[2]

Abstract— As small legged robots for search and rescue are deployed in collapsed buildings with unstructured terrain and steep drop-offs, they run the risk of flipping over and becoming incapacitated. A single degree of freedom low-mass tail is added to a 77.5 g, 18 cm long VelociRoACH legged robot with protective shell, which gives it the capability to dynamically self-right. Quasi-static analysis of terrestrial self-righting gives design requirements for the tail actuator. Dynamic simulation predicts that terrestrial self-righting is slower than aerial self-righting with a massive tail, but can be achieved without adding significant mass away from the base of leg support. Open-loop experiments on terrain with varying friction and roughness show that VelociRoACH can dynamically self-right using tail contact in as little time as 256 ms. Finally, an autonomous self-righting experiment on an obstacle with multiple step drops demonstrates that the robot can detect inversion and rapidly self-right while walking on challenging terrain.

I. INTRODUCTION

Decimeter-scale underactuated legged robots including VelociRoACH [1] have demonstrated high-speed locomotion over various terrain types. Moreover, these robots can be rapidly manufactured through the scaled Smart Composite Microstructures (SCM) process [2]. Due to their small size, high mobility, and ease of manufacture, SCM legged robots have potential as search and rescue aids in disaster scenarios. Previous work showed that thermoformed shells can protect SCM robots from falls [3], but recovering from inversion requires additional actuation. A protective shell and tail actuated by a single motor have been added to VelociRoACH (pictured in Fig. 1), which enable it to withstand falls on challenging terrain and then self-right.

Terrestrial robots often need to self-right while moving on unstructured terrain. One approach to self-righting is to design a robot's shape so that it passively reorients to a righted configuration, which can be achieved using the capture regions analysis developed by Kriegman [4]. However, this method can produce robot geometries that are too cumbersome for locomotion through tight spaces. Another self-righting design approach is to make a symmetric robot that can operate while inverted, such as RHex [5].

Active methods for self-righting require coordination of a robot's actuators. Kovač designed a robot that shifts its center

[1]Carlos S. Casarez is with the Department of Mechanical Engineering, University of California, Berkeley, CA 94720 USA. casarezc@berkeley.edu

[2] Ronald S. Fearing is with the Department of Electrical Engineering and Computer Sciences, University of California, Berkeley, CA 94720 USA. ronf@eecs.berkeley.edu
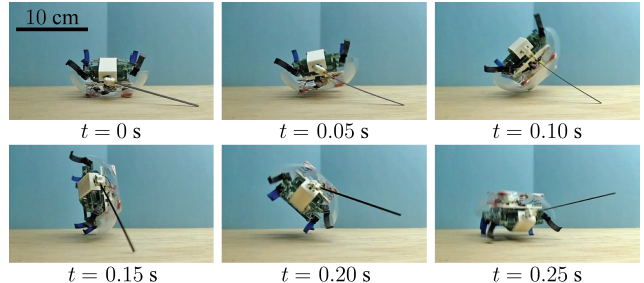
Fig. 1. High-speed camera frame sequence of a VelociRoACH robot with shell and active tail performing a dynamic self-righting maneuver on wood.

of mass and tips onto its legs before jumping [6]. Kessens developed a quasi-static framework for contact planning with actuated limbs that change a robot's convex hull to reorient on sloped surfaces [7]. An extension of this work established a self-rightability metric based on potential energy barriers to righting [8]. Active self-righting strategies that leverage dynamic maneuvers have also been demonstrated. Yamafuji analyzed the falling cat postural control problem and built a robot that could self-right in the air [9]. Saranli controlled the six leg actuators of RHex within a multi-contact dynamic framework to execute a flip about its pitch axis [10].

Several roboticists have taken inspiration from animal appendages for dynamic self-righting. Libby, Chang-Siu, and Johnson et al. analyzed and tested a lizard-inspired strategy for aerial self-righting, in which a robot pushes on the inertia of a massive tail to reorient its body [11], [12], [13]. Krummel designed a horseshoe crab robot that can self-right in surf zones by pushing its tail against the ground [14]. Li et al. demonstrated cockroach-inspired terrestrial self-righting with servomotor-driven wings [15].

Previous research on using tails for dynamic maneuvers focuses on the inertial effect of swinging a tail. TaylRoACH swings a yaw tail while running to produce high-speed transient turns on low-friction surfaces [16] and the Dima wheeled robot controls the motion of a roll tail to turn with increased maneuverability [17]. An inertial tail on the MIT Cheetah can be used to rapidly turn and reject impulsive disturbances [18]. Liu implemented a tail on a kangaroo-inspired hopping robot that balances angular momentum to limit pitch oscillations [19] and Kim showed that a water-running robot can cyclically move an inertial tail to stabilize roll oscillations of the body [20]. Although inertial tail maneuvers can be effective for reorientation and stabilization, they require a significant mass to be placed away from the base of leg support, which may hinder locomotion.

There has been limited research on using tail contact to assist locomotion. The dinosaur-like TITRUS-III robot uses

tail ground contact to stabilize quasi-static gaits [21]. Several robots, including Scout [22] and RiSE [23], have an extended passive tail to prevent pitch-back. Seo designed a tracked robot that pushes with an active tail to stabilize climbing and transition between orthogonal surfaces [24]. Brill explored the hybrid dynamics of the tailed Jerboa robot to find empirical contact sequences that lead to high jumps and significant horizontal gap crossings [25]. O'Connor discovered that kangaroos use their tail to propel and power low-speed locomotion in a pentapedal gait [26]. With a minimal tail that pushes against the ground, VelociRoACH can recover from inversion and could also potentially improve its capability to stabilize locomotion and execute transient jumps or turns.

This paper provides both analytic and experimental contributions towards understanding the terrestrial self-righting capability that a single degree of freedom tail gives a legged robot. A dynamic model is developed for terrestrial tailed righting with frictional contact. Terrestrial self-righting with an active tail is then tested using a VelociRoACH robot with shell on a range of surfaces and autonomous righting is demonstrated on terrain with steep drop-offs.

The paper is organized as follows: Section II develops a dynamic model of terrestrial righting with a tail driven by a single motor, gives tail design requirements for self-righting, and uses dynamic simulation to predict the time required to self-right. Section III details the results of experiments testing open-loop and autonomous terrestrial self-righting with a tail. Section IV compares the robot system to previous robots capable of self-righting and presents future directions.

II. Terrestrial Tailed Righting Analysis

A. Model parameters

For the dynamic model of tailed self-righting, Fig. 2a shows the mass and geometry parameters of a VelociRoACH robot with shell and tail. The robot body with shell has mass m_b and mass moment of inertia about its roll axis J_b. The robot without shell has overall width w and overall height h. The robot's rigidly mounted shell is approximated as half an ellipse in the roll plane of the robot, with major axis radius along the width of the robot r_w, minor axis radius along the height of the robot r_h, and center offset height above the center of mass (C.o.M.) of the robot h_c.

A rigid tail is driven by a motor in the roll plane of the robot, with an assumed pivot point about the C.o.M. for simplicity of analysis. The tail has mass m_t and mass moment of inertia about its C.o.M. J_t. The tail C.o.M. is located a distance $l_{G,t}$ from the tail pivot. Overlaid video frames of the VelociRoACH robot used in experiments swinging its tail are shown in Fig. 2b. Model parameters for this robot platform are given in Table I.

B. Newtonian dynamics formulation

Fig. 3 shows free body diagrams of tail-assisted self-righting. The analysis of self-righting is performed in the roll plane of the robot with world-fixed Cartesian frame $\{\mathbf{E_1}, \mathbf{E_2}, \mathbf{E_3}\}$. The forces acting on the system include gravity ($\mathbf{g} = -g\mathbf{E_2}$, $g = 9.81$ m/s^2), body contact force $\mathbf{F_b}$,
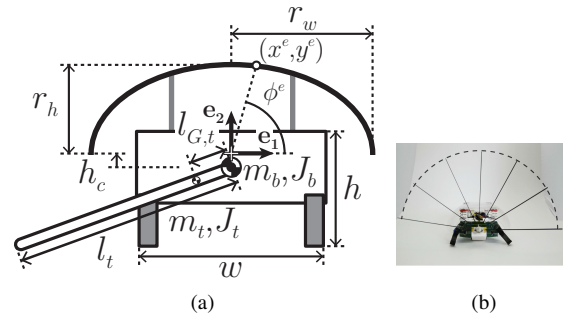

(a) (b)

Fig. 2. (a) Back view diagram showing mass and geometry parameters of a VelociRoACH robot with shell and active tail. (b) Overlaid video frames of VelociRoACH swinging its tail.

TABLE I
VelociRoACH with shell and tail parameters

Parameter name	Symbol	Value
Body mass	m_b	76.7 g
Body mass moment of inertia	J_b	583 g-cm^2
Overall width, height	(w, h)	(7.5, 4.5) cm
Shell major, minor axis radius	(r_w, r_h)	(5.5, 3.5) cm
Shell center offset height	h_c	0 cm
Tail mass	m_t	0.8 g
Tail mass moment of inertia	J_t	135 g-cm^2
Tail length, C.o.M. distance	$(l_t, l_{G,t})$	(9, 1.5) cm
Tail stall torque	τ_s	29.5 mN-m
Tail no-load speed	ω_{nl}	77 rad/s

and tail contact force $\mathbf{F_t}$. In Fig. 3a, $m = m_b + m_t$ is the total system mass. The net inertial force due to linear acceleration of the system C.o.M. is $-M\mathbf{a_G} = -m_b\mathbf{a_{G,b}} - m_t\mathbf{a_{G,t}}$.

For a given body roll angle θ_b relative to $\mathbf{E_1}$, the kinematics of a rolling ellipse provide constraints on the velocity and acceleration of the robot body. Fig. 2a shows the coordinates (x^e, y^e) of a point on the ellipse shell in the frame of the ellipse $\{\mathbf{e_1}, \mathbf{e_2}\}$. This point is located at an angle ϕ^e relative to $\mathbf{e_1}$. Using an alternate angle parameter ϕ satisfying $\tan\phi = \frac{r_h}{r_w}\tan\phi^e$, the body contact coordinates from the ellipse center in the frame of the ellipse are:

$$x_{P,b}^e = r_w \cos\phi \qquad (1)$$

$$y_{P,b}^e = r_h \sin\phi \qquad (2)$$

$$\phi = \tan^{-1}\left(\frac{r_h}{r_w \tan\theta_b}\right). \qquad (3)$$

For contact with the ellipse shell, the value of ϕ as a function of θ_b is determined from the tangency condition (3), which ensures that the tangent vector to the ellipse points along the horizontal $\mathbf{E_1}$. These contact coordinates are valid for counterclockwise righting with $\theta_b \in [0°, 90°]$. For body angles greater than $90°$, the robot is assumed to rotate about the edge of the shell. A rotation is applied to transform the contact displacements into the world-fixed Cartesian frame:

$$\mathbf{r_{P,b/G,b}} = \left(-x_{P,b}^e \cos\theta_b + \left(y_{P,b}^e + h_c\right)\sin\theta_b\right)\mathbf{E_1} \\ - \left(\left(y_{P,b}^e + h_c\right)\cos\theta_b + x_{P,b}^e \sin\theta_b\right)\mathbf{E_2}. \qquad (4)$$

In (4), the notation $\mathbf{r_{P,b/G,b}}$ indicates the position vector pointing from the body C.o.M. to the body contact point. In the following equations, the subscripts $\mathbf{P,b}$ and $\mathbf{P,t}$ refer to body and tail contact points. The subscripts $\mathbf{G,b}$ and $\mathbf{G,t}$
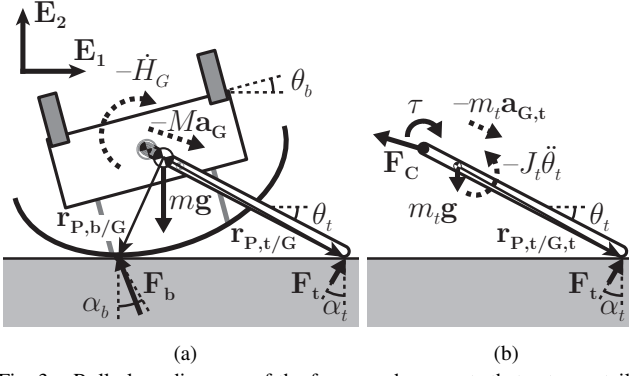
Fig. 3. Roll plane diagrams of the forces and moments that act on a tailed robot during a dynamic self-righting maneuver. (a) Free body diagram of the overall system and (b) free body diagram of the tail.

refer to body and tail C.o.M. points. The subscript $\mathbf{G}$ refers to the system C.o.M. Assuming zero velocity at the body contact, the constrained velocity of the body C.o.M. is:

$$\mathbf{v_{G,b}} = \dot{\theta}_b \mathbf{E_3} \times (-\mathbf{r_{P,b/G,b}}). \tag{5}$$

Differentiating (5) with respect to time results in an expression for the body C.o.M. acceleration $\mathbf{a_{G,b}}$ in terms of body angle θ_b and its time derivatives $(\dot{\theta}_b, \ddot{\theta}_b)$.

Because the rigid tail is assumed to maintain contact with the ground, the tail angle θ_t relative to $\mathbf{E_1}$ and its time derivatives $(\dot{\theta}_t, \ddot{\theta}_t)$ can be written in terms of the body angle:

$$\theta_t = \sin^{-1}\left(\frac{\mathbf{r_{P,b/G,b}} \cdot \mathbf{E_2}}{l_t}\right) \tag{6}$$

$$\dot{\theta}_t = -\frac{\mathbf{v_{G,b}} \cdot \mathbf{E_2}}{l_t \cos \theta_t} \tag{7}$$

$$\ddot{\theta}_t = -\left(\frac{\mathbf{v_{G,b}} \cdot \mathbf{E_2}}{l_t \cos^2 \theta_t}\dot{\theta}_t \sin \theta_t + \frac{\mathbf{a_{G,b}} \cdot \mathbf{E_2}}{l_t \cos \theta_t}\right), \tag{8}$$

where (6) comes from setting the tail height $l_t \sin \theta_t$ equal to $\mathbf{r_{P,b/G,b}} \cdot \mathbf{E_2}$, (7) comes from enforcing zero tail contact velocity in the $\mathbf{E_2}$ direction, and (8) comes from differentiating (7) with respect to time. Now, an expression for the linear acceleration of the tail C.o.M. can be determined:

$$\mathbf{a_{G,t}} = \mathbf{a_{G,b}} + \ddot{\theta}_t \mathbf{E_3} \times l_{G,t} (\cos \theta_t \mathbf{E_1} + \sin \theta_t \mathbf{E_2})$$
$$+ \dot{\theta}_t \mathbf{E_3} \times l_{G,t} \dot{\theta}_t (-\sin \theta_t \mathbf{E_1} + \cos \theta_t \mathbf{E_2}). \tag{9}$$

The linear momentum balance for the overall system is:

$$m_b \mathbf{a_{G,b}} + m_t \mathbf{a_{G,t}} = (m_b + m_t)\mathbf{g} + \mathbf{F_b} + \mathbf{F_t}. \tag{10}$$

For the overall system in Fig. 3a, (10) gives two linearly independent balance equations. An angular momentum balance for the overall system can also be written:

$$\dot{H}_G = J_b \ddot{\theta}_b + \left(J_t + \frac{m_b m_t}{m_b + m_t} l_{G,t}^2\right)\ddot{\theta}_t \tag{11}$$

$$\dot{H}_G \mathbf{E_3} = \mathbf{r_{P,b/G}} \times \mathbf{F_b} + \mathbf{r_{P,t/G}} \times \mathbf{F_t}, \tag{12}$$

where (11) is the time derivative of the system angular momentum about the C.o.M. and (12) is an angular momentum

balance considering the external forces acting on the system. The displacement vectors in (12) are given below:

$$\mathbf{r_{P,b/G}} = \mathbf{r_{P,b/G,b}} - \mathbf{r_{G/G,b}} \tag{13}$$

$$\mathbf{r_{P,t/G}} = \mathbf{r_{P,t/G,b}} - \mathbf{r_{G/G,b}} \tag{14}$$

$$\mathbf{r_{P,t/G,b}} = l_t (\cos \theta_t \mathbf{E_1} + \sin \theta_t \mathbf{E_2}) \tag{15}$$

$$\mathbf{r_{G/G,b}} = \frac{m_t l_{G,t}}{m_b + m_t}(\cos \theta_t \mathbf{E_1} + \sin \theta_t \mathbf{E_2}). \tag{16}$$

The last equation to solve for the system dynamics results from an angular momentum balance for the tail depicted in Fig. 3b. The constraint force $\mathbf{F_C}$ at the tail pivot satisfies the linear momentum balance for the tail and is given below:

$$\mathbf{F_C} = -\mathbf{F_t} - m_t \mathbf{g} + m_t \mathbf{a_{G,t}}. \tag{17}$$

With this expression for $\mathbf{F_C}$, the angular momentum balance for the tail about its C.o.M. is:

$$J_t \ddot{\theta}_t \mathbf{E_3} = \tau \mathbf{E_3} + l_t (\cos \theta_t \mathbf{E_1} + \sin \theta_t \mathbf{E_2}) \times \mathbf{F_t}$$
$$- l_{G,t} (\cos \theta_t \mathbf{E_1} + \sin \theta_t \mathbf{E_2}) \times m_t (\mathbf{a_{G,t}} - \mathbf{g}), \tag{18}$$

where τ is the input torque from a DC motor, which linearly decreases in magnitude with relative tail velocity $\dot{\theta}_t - \dot{\theta}_b$:

$$\tau = \begin{cases} -\tau_s \left(1 + \frac{\dot{\theta}_t - \dot{\theta}_b}{\omega_{nl}}\right), & \dot{\theta}_t - \dot{\theta}_b < 0 \\ -\tau_s, & \dot{\theta}_t - \dot{\theta}_b \geq 0. \end{cases} \tag{19}$$

In (19), the tail motor rotates clockwise relative to the body with maximum control effort. The torque-speed relation is parameterized by stall torque τ_s and no-load speed ω_{nl}.

Now, in order to solve for the system dynamics, friction conditions are applied to the contact forces. Coulomb friction is assumed with equal static and kinetic friction coefficients. The body and tail can have different coefficients of friction μ_b and μ_t. In the case shown in Fig. 3, the body contact is rolling without slip, so both components of $\mathbf{F_b}$ are unknown and inside the static friction cone with friction angle α_b, where $\tan \alpha_b = \mu_b$. The tail contact is sliding, so the tail normal force $\mathbf{F_t} \cdot \mathbf{E_2}$ is unknown and $\mathbf{F_t}$ is directed along the sliding friction cone parameterized by μ_t:

$$\mathbf{F_t} \cdot \mathbf{E_1} = -\mu_t (\mathbf{F_t} \cdot \mathbf{E_2}) \operatorname{sign}(\mathbf{v_{P,t}} \cdot \mathbf{E_1}), \tag{20}$$

where $\mathbf{v_{P,t}}$ is the tail contact velocity. The five independent equations (8), $\mathbf{E_1}$ and $\mathbf{E_2}$ components of (10), (12), and (18) are linear in the unknowns $(\ddot{\theta}_b, \ddot{\theta}_t, \mathbf{F_b} \cdot \mathbf{E_1}, \mathbf{F_b} \cdot \mathbf{E_2}, \mathbf{F_t} \cdot \mathbf{E_2})$ and are solved to determine dynamics equations and constraint forces as a function of system state $(\theta_b, \dot{\theta}_b, \theta_t, \dot{\theta}_t)$. The nonlinear system of second-order differential equations for θ_b and θ_t are numerically simulated in a following subsection.

If the solution for $\mathbf{F_b}$ produces a result outside of the static friction cone, then the body contact is sliding with known $\mathbf{F_b} \cdot \mathbf{E_1}$, the $\mathbf{E_1}$ component of the roll without slip velocity constraint in (5) is relaxed, and additional states $(x, \dot{x})$ for the body C.o.M. horizontal displacement and velocity are added to the dynamics formulation. A similar procedure for deriving the dynamics equations follows, but now $(\dot{x}, \ddot{x})$ are included in the balance equations, resulting in three second-order differential equations for (θ_b, θ_t, x).

In the following subsections, quasi-static analysis gives minimum torque requirements for the tail motor, and the dynamic system is simulated to predict the time required for self-righting with tail contact.

C. Quasi-static design considerations

For quasi-static analysis of tail-assisted self-righting, the tail motor maintains static equilibrium throughout the righting process. The left-hand sides of the dynamics equations (10), (12), and (18) are zero, the body rolls without slip, the tail slides with Coulomb friction, and the unknowns are $(\tau, \mathbf{F_b} \cdot \mathbf{E_1}, \mathbf{F_b} \cdot \mathbf{E_2}, \mathbf{F_t} \cdot \mathbf{E_2})$. In quasi-static self-righting, the tail rotates the body from an inverted configuration ($\theta_b = 0°$) to a critical body angle ($\theta_b = \theta_b^*$). Past this critical body angle, the system C.o.M. is to the left of the body contact point and gravity tends to tip the robot onto its legs. The maximum tail motor torque over the range of admissible body angles provides a quasi-static limit on the stall torque τ_s required for tail-assisted self-righting on a horizontal surface.

First, the quasi-static tail torque required for self-righting is determined for varying tail length l_t and varying coefficient of friction $\mu = \mu_b = \mu_t$, with remaining parameters fixed at the values in Table I. These results are plotted in Fig. 4a. Over the range of tail lengths, the tail torque required increases with μ. For tail-ground interactions with no friction ($\mu = 0$), torque required increases with tail length. Shorter tails result in contact angles that are more aligned with the vertical contact force in the zero friction case, which results in a smaller torque required to move the tail. For tail-ground interactions with high friction ($\mu = 1$), the relationship between tail torque required and tail length is inverted. Because of the high friction resisting lateral motion of the tail slipping against the ground, shorter tails result in a larger tail torque requirement. For tail-ground interactions with moderate friction ($\mu = 0.5$), tail length has a relatively minor effect on tail torque. In order to reduce the tail torque required to self-right on high-friction surfaces, a tail length of $l_t = 9$ cm was selected for VelociRoACH.

Next, the tail and friction parameters of the quasi-static model are held constant while the shell minor axis radius r_h and the shell offset height above the C.o.M. of the robot h_c are varied. As shown in Fig. 4b, the tail torque required for self-righting decreases as r_h and h_c increase. As r_h approaches r_w in the $h_c = 0$ case (circular shell shape), all contact configurations on the robot shell become unstable, and the robot tends to tip towards its legs with no applied tail torque. The shape variation results suggest that the shell should extend as high as possible above the C.o.M. of the robot to reduce tail motor torque requirements for self-righting. However, increasing the overall height of the robot can prevent the robot from entering low-clearance structures. This size constraint limits the shell height parameters of VelociRoACH to $r_h = 3.5$ cm and $h_c = 0$.

Based on the quasi-static analysis, a 30:1 reduction gearmotor (*Pololu*) was selected to drive the tail, which has an output stall torque of $\tau_s = 29.5$ mN-m and a no-load speed of $\omega_{nl} = 77$ rad/s at a voltage of 3.7 V. This motor provides
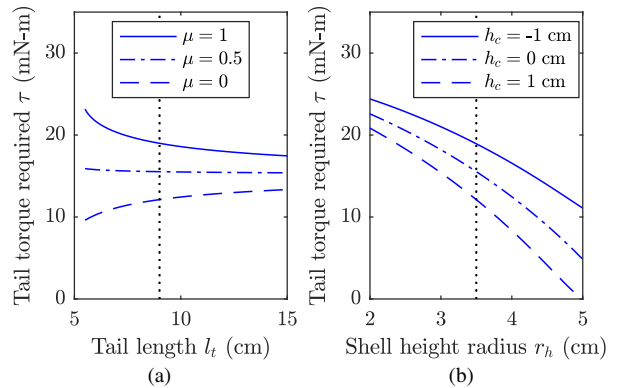

Fig. 4. Tail torque required for quasi-static self-righting of a robot with an elliptical shell on flat terrain. (a) Varying tail length and tail-ground sliding coefficient of friction, with robot shell parameters held constant at $r_h = 3.5$ cm and $h_c = 0$. (b) Varying shell height radius and shell offset height above the C.o.M., with $l_t = 9$ cm and $\mu = 0.5$.

enough torque for the robot to quasi-statically self-right on flat terrain over the range of considered friction conditions.

D. Dynamic righting time predictions

The system of second-order differential equations governing tail-assisted self-righting dynamics was numerically simulated using `ode45` in MATLAB, with events handling transitions between sliding and sticking contacts as well as detecting loss of contact when normal forces reach zero. The initial conditions are $(\theta_b, \dot{\theta}_b, \theta_t, \dot{\theta}_t)|_{t=0} = (0, 0, \theta_{t0}, 0)$, where θ_{t0} satisfies (6) with $\theta_b = 0$.

The results of the simulation for a wood surface ($\mu_b = 0.4$, $\mu_t = 0.5$) are shown in Fig. 5. A negative applied tail torque rotates the tail clockwise as the body accelerates counterclockwise. For this simulation case, the rolling body contact slips in the $\mathbf{E_1}$ direction and the tail contact slips in the $-\mathbf{E_1}$ direction. This relative motion produces negative horizontal body forces and positive horizontal tail forces. The tail normal force remains relatively constant (from 31% to 39% of the robot weight), and the body normal force reaches a peak of 112% of the robot weight at time $t = 0.035$ s.

At time $t = 0.134$ s, the body and tail lose contact with the ground, and are assumed to have constant angular velocity until the robot is fully righted with $\theta_b = 180°$. The righting performance is quantified by the elapsed time, $t_r = 235$ ms.

The dynamic simulation's prediction of terrestrial righting time is now compared to aerial righting. Fig. 6a shows the time t_r to complete aerial righting determined from the model in [13] for varying tail length l_t and tail end mass m_t. For aerial righting, t_r decreases as l_t and m_t increase (which increases the inertial leverage of the tail), with greater effects on t_r for tails with l_t ranging from 5 cm to 10 cm.

Assuming uniform friction ($\mu = \mu_b = \mu_t$), the dynamic simulation was used to predict the terrestrial righting time for varying tail length l_t and coefficient of friction μ. In contrast to aerial righting, the terrestrial righting time results in Fig. 6b show that t_r does not change much with varying l_t. The greatest effect of tail length is observed in the $\mu = 0.5$ case, in which increasing l_t from 7 cm to 15 cm
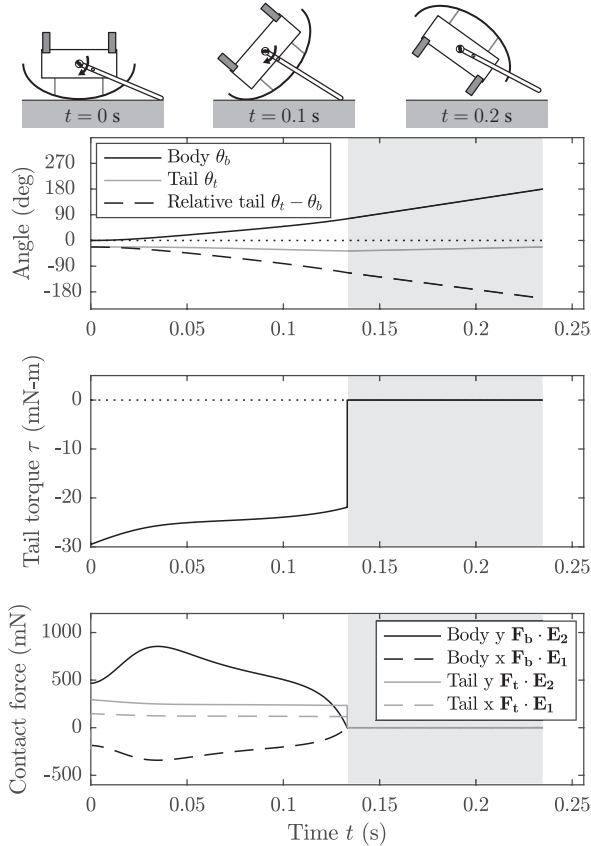
Fig. 5. Tail-assisted self-righting dynamic simulation results on flat ground with Coulomb friction at the shell and tail contacts. The body and tail coefficients of friction are $\mu_b = 0.4$ and $\mu_t = 0.5$. The shaded time interval indicates the loss of body and tail ground contact.

Fig. 6. Comparison of the time to perform a $180°$ roll reorientation of a robot body for (a) aerial self-righting with an inertial tail of varying mass and length and (b) terrestrial righting with a low-mass tail of varying length on surfaces with varying coefficient of friction $\mu = \mu_b = \mu_t$.

Fig. 7. Annotated image of VelociRoACH with protective shell and tail.

increases t_r by 37 ms. Righting time is far more sensitive to the coefficient of friction μ—for a tail length $l_t = 9$ cm, increasing μ from 0.3 to 0.7 increases t_r by 90 ms. Overall, terrestrial righting over the range of l_t and μ values takes 84–174 ms more time than the fastest aerial righting case.

III. TERRESTRIAL TAILED RIGHTING EXPERIMENTS

A. Robot platform

The legged robot in Fig. 7 was developed for tail-assisted self-righting experiments. The base platform is a modified VelociRoACH robot [1] with a mass of 53.6 g. The robot is powered by a single cell 300 mAh LiPo battery (*Lectron Pro*). The kinematic linkages of the robot have PET plastic as the structural material and ripstop nylon as the flexural material. To drive the robot legs with added payload, the leg transmissions have four times the torque capability of the original VelociRoACH, at the expense of a four times reduction in stride frequency. The robot has a 0.254 mm thick protective polycarbonate shell (adds 10.6 g) and a tail motor (*Pololu* 30:1 reduction high power micro metal gearmotor) that drives an interchangeable tail (adds 13.3 g). The total mass of the robot with added shell and tail is 77.5 g.

The tail is a flat carbon fiber beam (0.8 g with shaft attachment) with a width of 3 mm and a length of 10 cm. Because the tail motor is angled upward and the tail rotates along a cone, the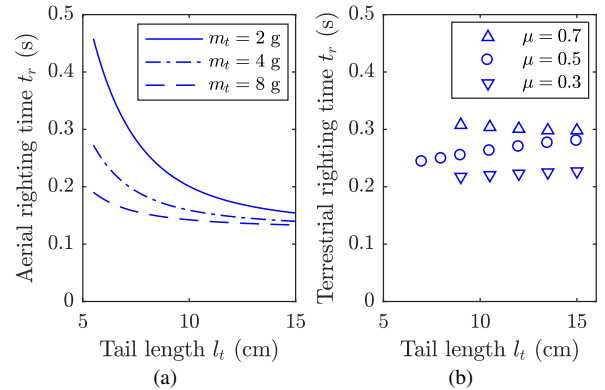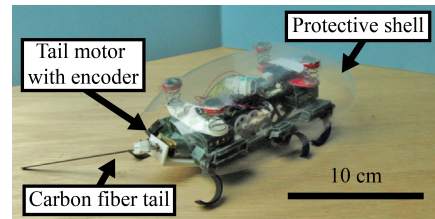 effective tail length in the roll plane of the robot is 9 cm. The high stiffness and low mass of the carbon fiber tail is well-matched to the self-righting model, which isolates the effect of generating ground contact forces with a tail from the inertial effect of swinging a massive tail.

B. Open-loop self-righting performance tests

The self-righting performance of VelociRoACH was tested by executing an open-loop tail control sequence while inverted. A sequence of high-speed video frames (taken at 300 fps) are shown for a representative open-loop self-righting trial in Fig. 1. In this experiment, the robot started inverted on a flat wood surface with its tail against the ground. Using a PID controller with feedback on tail position (measured with a magnetic rotary encoder), the robot applied an input voltage to swing its tail $180°$ clockwise. As pictured in the frame sequence, the tail pushes against the ground, causing the robot body to roll counterclockwise and self-right.

Telemetry data for ten repeated open-loop self-righting trials on wood are shown in Fig. 8. The telemetry plots show the time trajectories of the body roll angle (measured using the onboard accelerometer and gyroscope), the tail rotation angle relative to the body (the zero reference for θ_t is the initial contact angle), and the tail torque. The tail torque is calculated using (19) and the tail encoder measurements.

The leftmost vertical dotted line marks the start of righting. At this time, the tail torque decays from a maximum magnitude as the tail rotates clockwise and the body rotates counterclockwise. The middle dotted line marks the end of the period of useful tail work. After this time, the tail leaves the ground and the applied torque repositions the tail towards the desired angle $\theta_t - \theta_b = 180°$. Since the tail
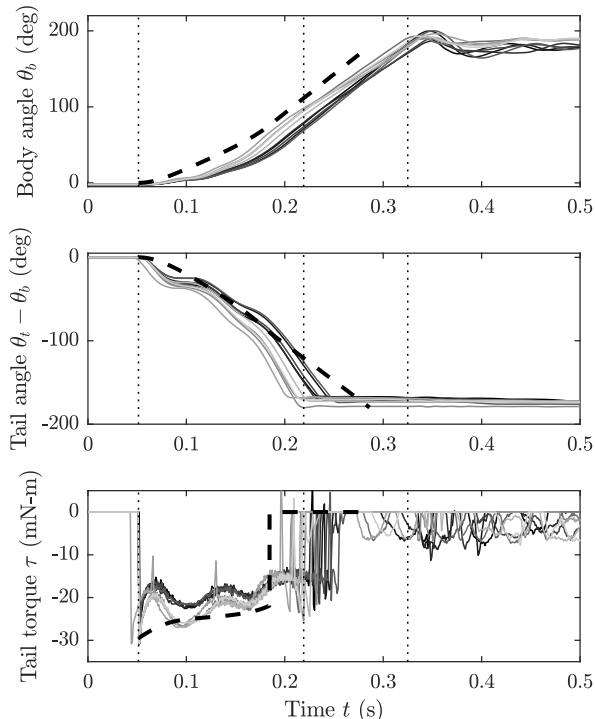
Fig. 8. Robot telemetry for ten repeated trials of open-loop tail-assisted self-righting on wood. The vertical dotted black lines mark the start of righting, the end of the period of tail work, and the end of righting. The dashed black line is the dynamic simulation result.

Fig. 9. Surfaces used in open-loop tail-assisted self-righting experiments.

TABLE II
TAIL-ASSISTED RIGHTING PERFORMANCE ON VARIOUS SURFACES

Surface	C.o.F. μ_b/μ_t	Model t_r (ms)	Experiment t_r (ms)	Successes
Wood	0.4/0.5	235	274 ± 7.71	10/10
Polystyrene	0.3/0.3	217	264 ± 15.8	10/10
Tile	0.35/0.45	226	336 ± 51.7	10/10
Low-pile carpet	0.25/1	214*	259 ± 41.3	10/10
High-pile carpet	0.35/1	229*	256 ± 35.0	10/10
Fixed rocks	0.35/1.2	231*	292 ± 65.8	9/10
Loose rocks	0.35/1.2	231*	358 ± 138	8/10

has little inertial leverage, it no longer accelerates the body, as indicated by the linear increase in body angle after this time. The rightmost dotted line marks the average time at which the body reaches $180°$. After this time, the left legs impact the ground and the robot settles onto its legs. For the wood surface experiments, the average righting time was 274 ms, with a standard deviation of 7.71 ms. Compared to the dashed simulation result ($\mu_b = 0.4$, $\mu_t = 0.5$), open-loop self-righting on wood was on average 41 ms slower. The planar model may underpredict righting time because in the experiments, the tail produced pitch and yaw motions outside of the roll plane. These higher dimensional dynamics could contribute to the more gradual roll angle acceleration of the robot body in the experiments relative to the model.

Open-loop tail-assisted self-righting was tested on the seven surfaces shown in Fig. 9. Table II shows experiment righting times (average $\pm$ standard deviation) and success rates over ten trials for self-righting on each surface. The surface friction coefficients were determined from inclined plane tests measuring static friction—body friction μ_b was measured for the polycarbonate shell on the surface, and tail friction μ_t was measured for the polyurethane C-legs of the robot on the surface. The C-leg friction measurement approximates the increased effective friction of the tail from engaging surfaces with significant roughness (e.g. carpet and rock surfaces). The righting times from the dynamic simulation are also shown. Note that the model results with an asterisk had modified initial conditions—due to the high tail friction, the simulation executions from zero initial velocity resulted in a sticking tail with non-physical contact
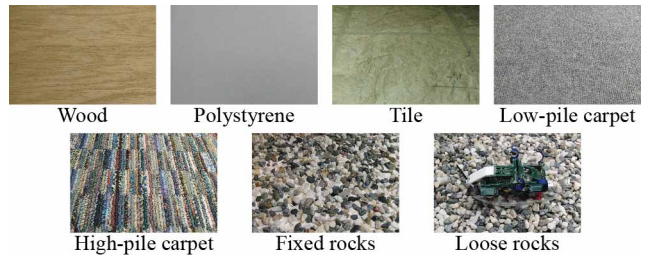
forces. In order to numerically resolve these simulation cases, an initial horizontal velocity of $\dot{x}(0) = 12.5$ cm/s was used, which is up to 13% of the maximum body slip velocity.

For the more uniform wood, polystyrene, and carpet surfaces, lower body friction and higher tail friction are correlated with faster righting times. The fastest average righting time was on high-pile carpet ($t_r = 256$ ms). For the wood, polystyrene, and low-pile carpet surfaces, the simulation matches the trend in righting times, but consistently underpredicts righting times by 39–47 ms.

The surfaces with more variation in roughness and appearance (tile, fixed rocks, loose rocks) had the highest average righting times with relatively large spreads across the ten trials. The tile surface has millimeter-scale surface variations and the rock surfaces have centimeter-scale rocks either fixed in a single layer or loosely packed in multiple layers. Due to the variability of these surfaces, the tail can intermittently lose surface contact, which results in slower average righting times than predicted by the model. For the fixed and loose rock surfaces, the loss of tail effectiveness was sometimes so severe that the robot failed to right. In these failure cases, the robot could still swing its tail again in another self-righting attempt. Refer to the video attachment for high-speed video of successful self-righting on wood, low-pile carpet, tile, and loose rocks as well as failed self-righting on loose rocks.

C. Autonomous self-righting reflex on unstructured terrain

In addition to open-loop tests of tail-assisted self-righting, an autonomous self-righting reflex was demonstrated as VelociRoACH walked down a paper-covered obstacle with multiple step drops on the order of the robot's body length. The control strategy for this autonomous behavior is shown in the block diagram in Fig. 10. Telemetry data from the robot during this experiment is shown in Fig. 11 and a camera frame sequence is shown in Fig. 12 (also shown in the video attachment). With the robot's legs following a bounding gait with a stride frequency of 4 Hz, a pre-programmed
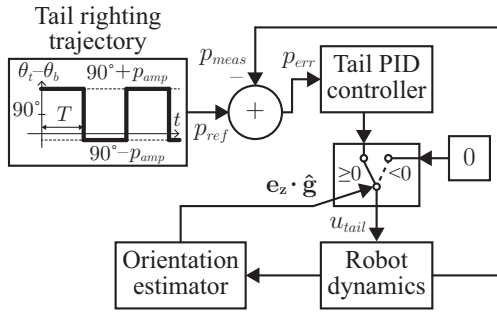
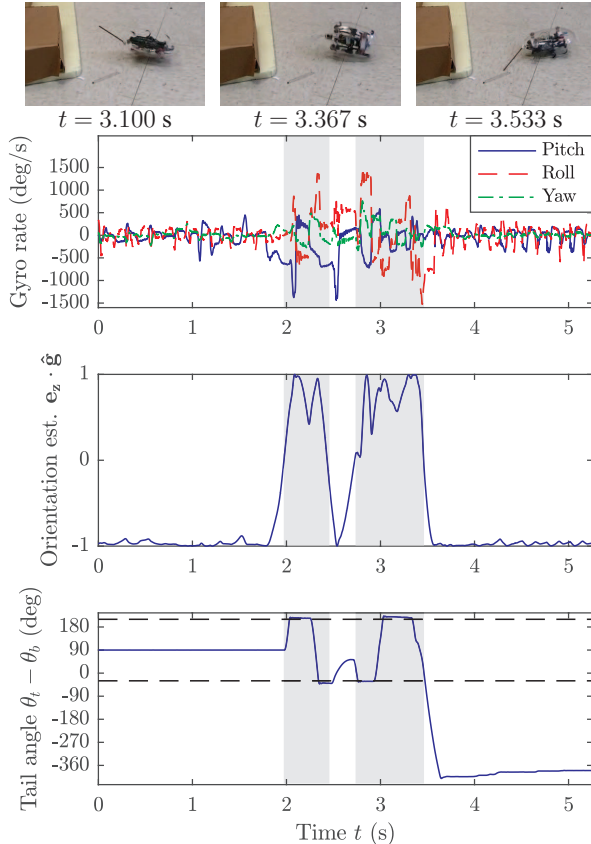Fig. 10. Autonomous tailed self-righting reflex control block diagram.

Fig. 11. Robot telemetry for an autonomous tailed self-righting reflex while walking down a step obstacle with a stride frequency of 4 Hz. The shaded time intervals are when the robot detects that it is inverted. In the tail angle plot, the dashed lines at $-30°$ and $210°$ indicate the target tail angles.

tail righting trajectory is activated during inversion. The trajectory p_{ref} periodically swings the tail over the top of the robot and is parameterized by the swing period $T = 0.4$ s and the swing amplitude $p_{amp} = 120°$ relative to the vertical tail position $\theta_t - \theta_b = 90°$. Using an onboard orientation estimator giving roll-pitch-yaw Euler angles (initialized with the accelerometer, then propagated forward in time with integrated gyroscope measurements), the tail PID controller is activated when the robot's body-fixed vertical vector $\mathbf{e_z}$ is aligned with the normalized gravity vector $\hat{\mathbf{g}}$. Using feedback on the tail position p_{meas}, the tail PID controller applies the motor control signal u_{tail} until the robot is upright.

As shown in Figs. 11 and 12, the autonomous self-righting reflex engages during locomotion whenever the robot's tum-
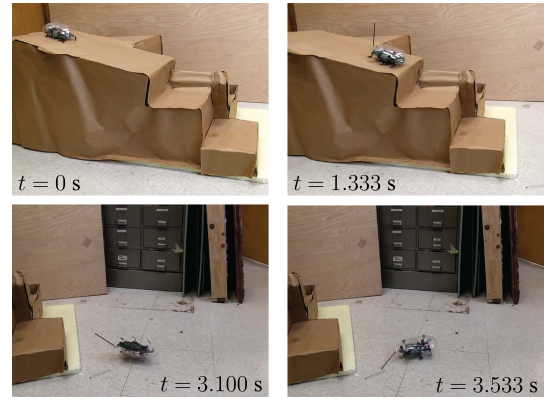

Fig. 12. Camera frame sequence of an autonomous tailed self-righting reflex after VelociRoACH walks off an obstacle with steep drop-offs.

bling motion causes it to invert. In the second shaded time interval of inversion, the robot successfully self-rights at the bottom of the obstacle and walks forward.

IV. DISCUSSION AND CONCLUSIONS

In conclusion, the analysis gives quasi-static torque requirements for sizing a tail and a tail motor for self-righting a ground robot. The dynamic simulation of terrestrial self-righting on flat terrain gives a reasonable prediction for the time required to self-right on uniform surfaces. Compared to aerial self-righting with an inertial tail of the same length and end mass ranging from 2.6% to 10.3% robot mass, terrestrial self-righting on wood (simulation righting time of 235 ms) is predicted to be 12 ms to 89 ms slower, while in experiments the robot took an additional 39 ms to self-right. An advantage of this self-righting strategy is that it can be performed with a tail that is only 1% of the robot's mass.

Experiments using a 77.5 g tailed VelociRoACH robot show that terrestrial self-righting can be consistently achieved with righting times as fast as 256 ms (with at least an 80% success rate after a single tail swing) on surfaces with different roughness scales and friction properties, including loose rocks. However, the dynamic simulation was unable to fully model the conditions of the experiments. In future work, the simulation will be improved through a 3D dynamics formulation that accounts for the pitch and yaw motions that the tail causes. In addition, a terradynamics model such as resistive force theory by Li et al. will be included to better model self-righting on granular terrain [27]. Self-righting through tail contact was demonstrated on flat terrain, but large obstacles compared to the robot could prevent successful self-righting, such as channels that are too narrow for the body to fully rotate and ledges that cause the tail to lose contact with the ground. Planned vibrational or contacting leg motions coordinated with tail motion could potentially self-right the robot from these challenging conditions.

The dynamic reorientation performance of the robot in this work is compared to other robot platforms with tail-like appendages in Table III. On flat surfaces of varying friction and moderately rough rock terrain, the presented robot performs a 180° roll reorientation faster than the other platforms that use inertial tails or tail contact to reorient about pitch, roll, or

TABLE III

COMPARISON OF ROBOTS WITH TAIL-LIKE APPENDAGES THAT CAN RAPIDLY REORIENT

Robot	Reorientation axis, method	Condition	Body inertia (kg-m^2)	Peak motor power (W)	Reorientation time (ms)	Angle (degrees)
Tailbot [13]	Pitch, inertial	Aerial	154×10^{-6}	4	128	90
RHex with tail [13]	Pitch, inertial	Aerial	0.15	50	350	90
TaYLRoACH [16]	Yaw, inertial	Low-friction surface	39.6×10^{-6}	2.5	250	90
Cockroach-inspired winged robot [15]	Pitch, contact	Flat surface	110×10^{-6}	0.88	600	180
Horseshoe crab robot [14]	Roll, contact	Surf zone	−	0.5	2000	180
VelociRoACH with tail (this work)	Roll, contact	Carpet, loose rocks	58.3×10^{-6}	0.57	$256, 358$	180

yaw axes. The mass moment of inertia about the reorientation axis and the peak mechanical motor power for self-righting are included as a means of comparison.

The demonstration of the autonomous tail-assisted self-righting reflex shows that VelociRoACH with tail is capable of detecting and recovering from inversion as it moves on complex terrain. However, switching to a prescribed righting strategy during inversion produced self-righting that was no faster than the open-loop righting results. In a continuation of this work, a control strategy will be developed to position the tail and produce torque in response to a measured disturbance, which can prevent inversion while running on rough terrain with varying slope. This feedback control strategy will exert control efforts that scale with disturbance magnitude and will decide to roll downhill instead of uphill to speed up righting. Finally, the potential of using a single degree of freedom low-mass tail for functions in addition to self-righting will be explored through control of the tail as an additional locomotion limb, further expanding the robot's mobility. Since the tail can apply large forces relative to the legs with a long moment arm, impulsive tail motions could produce significant vertical jumps to clear obstacles or produce rapid turns.

ACKNOWLEDGMENTS

REFERENCES

[1] D. W. Haldane, K. C. Peterson, F. L. Garcia Bermudez, and R. S. Fearing, "Animal-inspired design and aerodynamic stabilization of a hexapedal millirobot," in *IEEE ICRA*, May 2013, pp. 3279–3286.

[2] A. M. Hoover and R. S. Fearing, "Fast scale prototyping for folded millirobots," in *IEEE ICRA*, May 2008, pp. 886–892.

[3] D. W. Haldane, C. S. Casarez, J. T. Karras, J. Lee, C. Li, A. O. Pullin, E. W. Schaler, D. Yun, H. Ota, A. Javey, and R. S. Fearing, "Integrated manufacture of exoskeletons and sensing structures for folded millirobots," *J. Mech. Robot.*, vol. 7, no. 2, p. 021011, 2015.

[4] D. J. Kriegman, "Let them fall where they may: Capture regions of curved objects and polyhedra," *Int. J. Robot. Res.*, vol. 16, no. 4, pp. 448–472, 1997.

[5] U. Saranli, M. Buehler, and D. E. Koditschek, "RHex: A simple and highly mobile hexapod robot," *Int. J. Robot. Res.*, vol. 20, no. 7, pp. 616–631, 2001.

[6] M. Kovač, M. Schlegel, J.-C. Zufferey, and D. Floreano, "Steerable miniature jumping robot," *Autonomous Robots*, vol. 28, no. 3, pp. 295–306, 2010.

[7] C. C. Kessens, D. C. Smith, and P. R. Osteen, "A framework for autonomous self-righting of a generic robot on sloped planar surfaces," in *IEEE ICRA*, 2012, pp. 4724–4729.

[8] C. C. Kessens, C. T. Lennon, and J. Collins, "A metric for self-rightability and understanding its relationship to simple morphologies," in *IEEE/RSJ IROS*, 2014, pp. 3699–3704.

[9] K. Yamafuji, T. Kobayashi, and T. Kawamura, "Elucidation of twisting motion of a falling cat and its realization by a robot," *Journal of the Robotics Society of Japan*, vol. 10, no. 5, pp. 648–654, 1992.

[10] U. Saranli, A. A. Rizzi, and D. E. Koditschek, "Model-based dynamic self-righting maneuvers for a hexapedal robot," *Int. J. Robot. Res.*, vol. 23, no. 9, pp. 903–918, 2004.

[11] T. Libby, T. Y. Moore, E. Chang-Siu, D. Li, D. J. Cohen, A. Jusufi, and R. J. Full, "Tail-assisted pitch control in lizards, robots and dinosaurs," *Nature*, vol. 481, no. 7380, pp. 181–184, 2012.

[12] E. Chang-Siu, T. Libby, M. Brown, R. J. Full, and M. Tomizuka, "A nonlinear feedback controller for aerial self-righting by a tailed robot," in *IEEE ICRA*, 2013, pp. 32–39.

[13] T. Libby, A. M. Johnson, E. Chang-Siu, R. J. Full, and D. E. Koditschek, "Comparative design, scaling, and control of appendages for inertial reorientation," *IEEE Trans. Robot.*, vol. 32, no. 6, pp. 1380–1398, 2016.

[14] G. Krummel, K. N. Kaipa, and S. K. Gupta, "A horseshoe crab inspired surf zone robot with righting capabilities," in *ASME IDETC*, 2014.

[15] C. Li, C. C. Kessens, A. Young, R. S. Fearing, and R. J. Full, "Cockroach-inspired winged robot reveals principles of ground-based dynamic self-righting," in *IEEE/RSJ IROS*, 2016, pp. 2128–2134.

[16] N. J. Kohut, A. O. Pullin, D. W. Haldane, D. Zarrouk, and R. S. Fearing, "Precise dynamic turning of a 10 cm legged robot on a low friction surface using a tail," in *IEEE ICRA*, 2013, pp. 3299–3306.

[17] A. Patel and M. Braae, "Rapid turning at high-speed: Inspirations from the cheetah's tail," in *IEEE/RSJ IROS*, 2013, pp. 5506–5511.

[18] R. Briggs, J. Lee, M. Haberland, and S. Kim, "Tails in biomimetic design: Analysis, simulation, and experiment," in *IEEE/RSJ IROS*, 2012, pp. 1473–1480.

[19] G.-H. Liu, H.-Y. Lin, H.-Y. Lin, S.-T. Chen, and P.-C. Lin, "A bio-inspired hopping kangaroo robot with an active tail," *Journal of Bionic Engineering*, vol. 11, no. 4, pp. 541–555, 2014.

[20] H. G. Kim, D. G. Lee, and T. W. Seo, "Rolling stability enhancement via balancing tail for a water-running robot," *Journal of Bionic Engineering*, vol. 12, no. 3, pp. 395–405, 2015.

[21] K. Takita, T. Katayama, and S. Hirose, "The efficacy of the neck and tail of miniature dinosaur-like robot TITRUS-III," in *IEEE/RSJ IROS*, 2002, pp. 2593–2598.

[22] S. A. Stoeter, I. T. Burt, and N. Papanikolopoulos, "Scout robot motion model," in *IEEE ICRA*, 2003, pp. 90–95.

[23] M. Spenko, G. Haynes, J. Saunders, M. Cutkosky, A. Rizzi, R. Full, and D. Koditschek, "Biologically inspired climbing with a hexapedal robot," *J. Field Robot.*, vol. 25, no. 2008, pp. 223–242, 2008.

[24] T. Seo and M. Sitti, "Tank-like module-based climbing robot using passive compliant joints," *IEEE/ASME Transactions on Mechatronics*, vol. 18, no. 1, pp. 397–408, 2013.

[25] A. L. Brill, A. De, A. M. Johnson, and D. E. Koditschek, "Tail-assisted rigid and compliant legged leaping," in *IEEE/RSJ IROS*, 2015, pp. 6304–6311.

[26] S. M. O'Connor, T. J. Dawson, R. Kram, and J. M. Donelan, "The kangaroo's tail propels and powers pentapedal locomotion," *Biology Letters*, vol. 10, no. 7, p. 20140381, 2014.

[27] C. Li, T. Zhang, and D. I. Goldman, "A terradynamics of legged locomotion on granular media," *Science*, vol. 339, no. 6126, pp. 1408–1412, 2013.